Estimating Effective Leaf Area Index of Winter Wheat Using Simulated Observation on Unmanned Aerial Vehicle-Based Point Cloud Data

Yang Song, *Student Member, IEEE*, Jinfei Wang, *Member, IEEE*, and Jiali Shang, *Member, IEEE*

***Abstract*—Within-field variation of leaf area index (LAI) plays an essential role in field crop monitoring and yield forecasting. Although unmanned aerial vehicle (UAV)-based optical remote sensing method can overcome the spatial and temporal resolution limitations associated with satellite imagery for fine-scale within-field LAI estimation of field crops, image correction and calibration of UAV data are very challenging. In this study, a physical-based method was proposed to automatically calculate crop effective LAI (LAIe) using UAV-based 3-D point cloud data. Regular high spatial resolution RGB images were used to generate point cloud data for the study area. The proposed method, simulated observation of point cloud (SOPC), was designed to obtain the 3-D spatial distribution of vegetation and bare ground points and calculate the gap fraction and LAIe from a UAV-based 3-D point cloud dataset at vertical, 57.5°, and multiview angle of a winter wheat field in London, Ontario, Canada. Results revealed that the derived LAIe using the SOPC multiview angle method correlates well with the LAIe derived from ground digital hemispherical photography, $R^2 = 0.76$. The root mean square error and mean absolute error for the entire experiment period from May 11 to May 27 were 0.19 and 0.14, respectively. The newly proposed method performs well for LAIe estimation during the main leaf development stages (BBCH 20-39) of the growth cycle. This method has the potential to become an alternative approach for crop LAIe estimation without the need for ground-based reference measurements, hence save time and money.**

***Index Terms*—Agriculture, gap fraction, leaf area index (LAI), point cloud data, unmanned aerial vehicle (UAV), winter wheat.**

I. Introduction

REMOTE sensing offers an effective alternative for field data collection. The image data can be processed and analyzed to derive information for improving crop management decisions. In particular, high spatial and temporal resolution images can offer the spatial details and temporal frequencies for precision farming at the subfield scale. Leaf area index (LAI) is a critical vegetation descriptor that affects crop's interception of photosynthetic radiation, water transpiration, gas and energy exchange between plants and the Earth-atmosphere system [1]. LAI is identified as one half of the total green leaf area per unit horizontal ground surface area. It has been used in many crop growth models to predict other crop parameters including, chlorophyll content, biomass, and final yield [2]–[4]. Therefore, many remotely sensed studies have developed many methods based on different theories to estimate LAI for crop monitoring.

One of the most widely applied methods for LAI estimation is the empirical method using vegetation indices (VI) derived from multispectral or hyperspectral images [5], [6]. However, the determination of LAI using VI has many disadvantages.

1) VI methods are highly dependent on the radiation conditions at the time of imaging.
2) VI methods tend to saturate at high LAI values and dense vegetation canopy later in the crop growth season [7], [8].
3) The establishment of a regression relationship requires ground measurements during the calibration procedure.
4) The relationship between LAI and VIs is largely influenced by biological, geographical, and environmental conditions, which will require recalibration with the change of time and geographical locations [9].

Hence, the empirical method used to predict LAI over a large area is labor-intensive and time-consuming [10].

The spatial and temporal resolution of satellite imagery restricts the operational application of empirical methods to LAI monitoring for a single field. Due to the rapid development of UAV in recent years, many studies used a statistical method to estimate LAI from UAV-based multispectral images to overcome the spatial and temporal resolution restrictions of satellite imagery [11]–[13]. The UAV data can achieve long-term high spatial and temporal LAI monitoring for a single field, but the accuracy of the UAV-based multispectral image is affected by image radiometric correction and image alignment. Also, the UAV-based statistical method requires ground-based LAI measurement from numerous samples.

LAI has also been estimated from simulated physical models by establishing relationships between crop spectral information, canopy architecture, biophysical, and biochemical parameters [14], [15]. The remote sensing spectral information including reflectance and VIs were used as an input parameter for LAI estimation in the inversed simulated physical, such as radiative transfer models [16]–[18]. However, crop simulated

Manuscript received November 28, 2019; revised March 13, 2020; accepted May 6, 2020. Date of publication May 28, 2020; date of current version June 16, 2020. This work was supported in part by the NSERC discovering Grant awarded to Dr. Jinfei Wang, and in part by the Canadian Space Agency SOAR-E program under Grant SOAR-E-5489. *(Corresponding author: Yang Song.)*

Yang Song and Jinfei Wang are with the Western University, London, ON N6A5C2, Canada (e-mail: ysong24@uwo.ca; jfwang@uwo.ca).

Jiali Shang is with the Agriculture and Agri-Food Canada, Ottawa, ON K1A0C6, Canada (e-mail: jiali.shang@agr.gc.ca).

Digital Object Identifier 10.1109/JSTARS.2020.2995577

physical models require extensive ground measurements including weather conditions, vegetation structural properties, and biochemical parameters to simulate crop development. LAI estimation from simulated physical model inversion will also require these parameters which exclude the model from operational applications to large areas due to intensive ground data requirement. Furthermore, the quality of remote sensing data can also have a significant impact on the performance of the inversion.

Ground-based LAI measurements have often been used as a reference for model calibration and validation in many remote sensing studies. Two categories of ground measurement approaches, direct and indirect, have been used for field LAI estimation. The direct approach measures the actual leaf area using a destructive method, which is challenging for large areas and long-term LAI monitoring. The indirect approach retrieves effective LAI (LAIe) or actual LAI using nondestructive methods by measuring radiation transmittance through canopy using radiative transfer theories. The LAIe is one half of the total area of leaves that intercepts the light per unit horizontal ground surface area [10]. If the crop canopy satisfies the assumption of a random spatial distribution, the gap fraction in the canopy is equivalent to canopy transmittance. The LAIe can then be calculated from the canopy gap fraction [19]. The vertical and 57.5° gap fraction measurements obtained from digital color photography on the ground have been used for crop LAIe estimation under certain conditions, in which the vertical method requires assumptions on leaf angle distribution and 57.5° gap fraction method requires correction for the woody area and assume gaps can be measured. They achieved good agreement with the actual LAI measurements [19]–[22]. DHP is another approach to retrieve crop LAIe using the gap fraction measurements. DHP can be captured by a digital camera equipped with a fish-eye lens. The photographs are classified into vegetation and soil or vegetation and sky to calculate the gap fraction from different angles. The LAIe calculation can be achieved using specific DHP processing software such as CAN-EYE v6.4 [23] and Gap Light Analyzer v2.0 [24].

In addition to the optical gap fraction method, many studies have also attempted to use terrestrial laser scanning (TLS) derived 3-D point cloud data to estimate gap fraction or LAI of forest [25], [26]. The 3-D point cloud data models the forest canopy structure, which can then be used to retrieve the spatial distribution of foliage and LAIe. However, the method for using the TLS system can only estimate the LAI for a specific location, which is difficult for a large-scale LAI monitoring. Many studies have attempted to adopt airborne LiDAR to achieve forest LAI estimation [27], [28]. The LiDAR-derived LAI map was served as a reference for validating satellite LAI products at regional scales. Although airborne LiDAR could provide LAI maps for a small area, its high cost is a barrier to its wide-spread adoption for farm fields.

UAV has been recognized as an effective remote sensing platform for crop status monitoring over a single crop field. UAV-based photogrammetry can generate 3-D point cloud data similar to LiDAR, which contains crop structural information. Some studies have retrieved winter wheat height and vineyard structure using UAV-based point cloud data [29], [30]. However, to our best knowledge, there has been no reported application of using UAV-based 3-D crop structural information for winter wheat LAIe estimation. Therefore, the purpose of this research work was to explore the use of UAV-based 3-D point cloud data for winter wheat canopy LAIe estimation using ground-based gap fraction methods and the generation of LAIe map of a single crop field without the support of *in-situ* LAI measurements.

II. Methodology

A. LAIe Estimation Using Gap Fraction on UAV-Based Point Cloud Data

The gap fraction method was adopted as an indirect and noncontact method for canopy structure analysis. According to Poisson distribution, the relationship between canopy gap fraction and LAIe is given as follows [25]:

$$\mathrm{LAIe} = \frac{-\cos(\theta)\ln P(\theta)}{G(\theta)} = \frac{-\ln P(\theta)}{k(\theta)} \tag{1}$$

where $P(\theta)$ is the gap fraction at a certain view angle, LAIe is the estimated LAIe, $G(\theta)$is the fraction of foliage projected towards view angle θ.

The vertical gap fraction method estimates crop LAIe using vegetation cover fraction at the nadir view [20], [22]. This method adopted the gap fraction at zenith angle θ equal to 0°. Assuming the leaf angle distribution is uniform in azimuth, and following a spherical distribution for the inclination, the value of G is equal to 0.5 at any direction [20], [31]. The formula is shown in the following equation:

$$\mathrm{LAIe}_0 = -2\ln(P_0(0)) \tag{2}$$

where $P_0(\theta)$ is the gap fraction at a nadir direction, and eLAI_0 is the estimated LAIe using the vertical gap fraction measurement.

The method of gap fraction at zenith angle θ equal to 57.5° has been used to estimate crop LAIe [19], [21], [22]. Since the extinction coefficient k is dependent on the value of $G(\theta)$, when $G(\theta)$ is 0.5 at zenith angle 57.5°, the value of k is 0.93 correspondingly. The formula can be written as follows:

$$\mathrm{LAIe}_{57.5} = \frac{-\ln(P_0(57.5^\circ))}{0.93}. \tag{3}$$

According to the Beer-Lambert law that the distance of light traveled in the medium is proportional to the attenuation of light, the following equation gives the relationship between foliage density and the gap fraction of the crop canopy:

$$-\ln P(\theta) = G(\theta)\,\mu S(\theta) \tag{4}$$

where μ is the foliage density, and $S(\theta)$ is the pathlength through the canopy for each view angle θ. Miller [32] gives an exact solution for foliage density as shown in the following equation:

$$\mu = -2\int_0^{\pi/2} \frac{\ln(P(\theta))}{S(\theta)}\sin\theta d\theta. \tag{5}$$

For canopy structure such as corn and wheat, $S(\theta)$could be calculated from height z, which is $S(\theta) = z/\cos\theta$; and LAIe

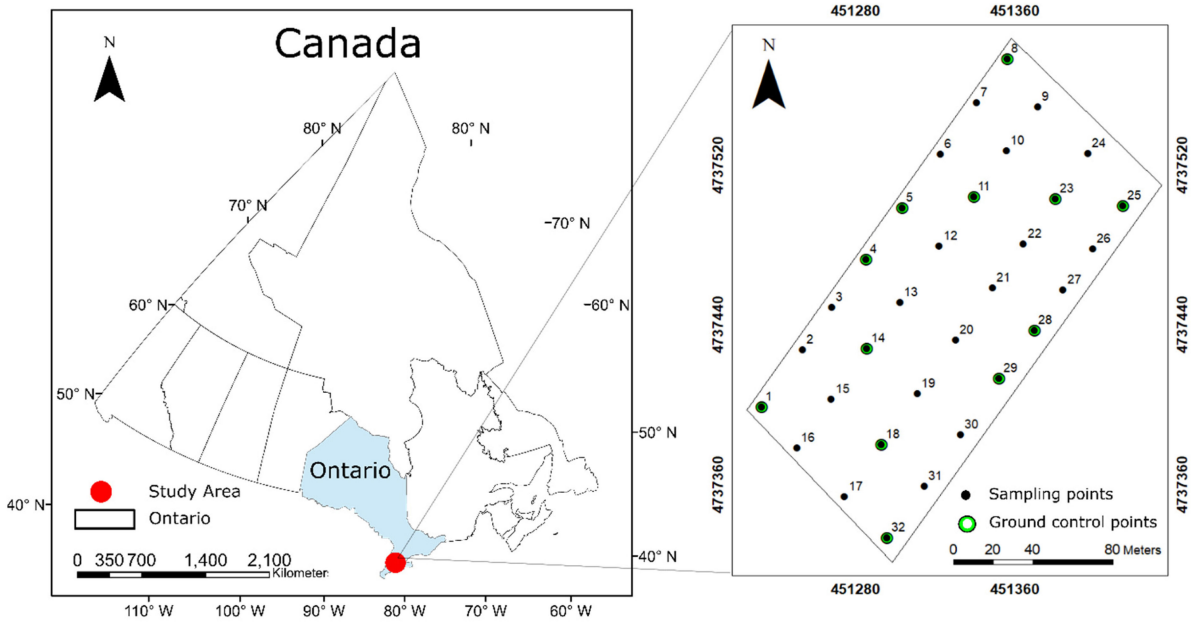

Fig. 1. Study area and sampling locations in the test field. (a) Study area in Melbourne, Ontario, Canada. (b) Sampling locations in the study area. The black points are the ground measurement location, and the green circles are the ground control points.

could be calculated from foliage density and canopy height, which is $\mu \times z$, so (2) can be rewritten as

$$\mathrm{LAIe} = -2\int_0^{\pi/2} \ln\left(P\left(\theta\right)\right)\cos\theta\sin\theta d\theta. \tag{6}$$

Many plant canopy devices such as LAI-2200 and fisheye camera used a hemispherical lens to measure the gap fraction at different zenith angles. LAI-2000 adopts five rings (7°, 23°, 38°, 53°, 68°) with a weighted sum approach to calculate LAIe. In our study, we adopted these observation angles and weight sum approach to calculate LAIe. The formula is shown in the following equation:

$$\mathrm{LAIe} = -2\sum_{i=1}^{5} \ln\left(P\left(\theta_i\right)\right)\cos\left(\theta_i\right)\sin\left(\theta_i\right)\Delta\theta_i \tag{7}$$

where θ_i is the centre zenith angle of the ring i and $\Delta\theta_i$ is the range of the zenith angles for this ring i.

This theory has been adopted by many studies and commercial devices to retrieve *in-situ* indirect LAIe measurements. This indirect LAIe measurement showed good performance on crops such as wheat and corn has been used as reference in many remote sensing studies [33]–[35].

B. Site Description and Ground-Based DHP Data Collection

The study site is a winter wheat field located in the west of Melbourne in southwest Ontario, Canada [see Fig. 1(a)]. Winter wheat in this region is usually planted in previous October and goes dormant in winter and continues to grow until the end of June, with a single harvest per year. Due to the cold spring in 2019, winter wheat had a late growing season and lasted till mid-July in this study site. A 120 × 240 m area was used to collect multitemporal ground-based LAI and UAV-based red, green, and blue (RGB) images from early May to mid-June. Thirty-two samples were collected along the row direction of the winter wheat to minimize the damage to crops by surveyors and ensure the quality of future UAV images. The locations of all sampling points are shown in Fig. 1(b). Gap fraction was measured on the ground using a nondestructive method with a Nikon D300s camera equipped with a 10.5 mm fisheye lens. At each sampling point, seven digital hemispherical photographs were taken at a downward direction for winter wheat canopy within a 2 × 2 m area. All photographs were captured with the lens held at 1 m above the top of the canopy. The CAN-EYE v6.4 software was used to process the DHPs to calculate the LAIe used in this study, and the hemispherical photo derived LAIe was used as a reference to validate UAV derived LAIe estimation. In addition, 12 black and white chess boards (2 by 2 cells) were set up at selected sampling points during the entire growing season. The size of the chess board is 1 ft by 1 ft and composed of two corresponding black and white rectangles at the size of 0.5 ft by 0.5 ft. These target boards were used as tie points for multitemporal UAV based point cloud datasets registration to ensure the accuracy of relative position among datasets. Their locations were shown as green circles over the sampling points in Fig. 1(b).

C. UAV Data Collection and Processing

Multitemporal UAV based imagery was collected using a DJI Phantom 4 RTK UAV system with a 5K high-resolution digital RGB camera and an RTK base station. The UAV flights were performed on cloud-free days between 10 A.M. and 2 P.M. to reduce the shadow influence on images. The UAV image processing software Pix4Dmapper Pro (Pix4D) v2.4 (Pix4D SA, Lausanne, Switzerland) was used to generate 3-D point cloud

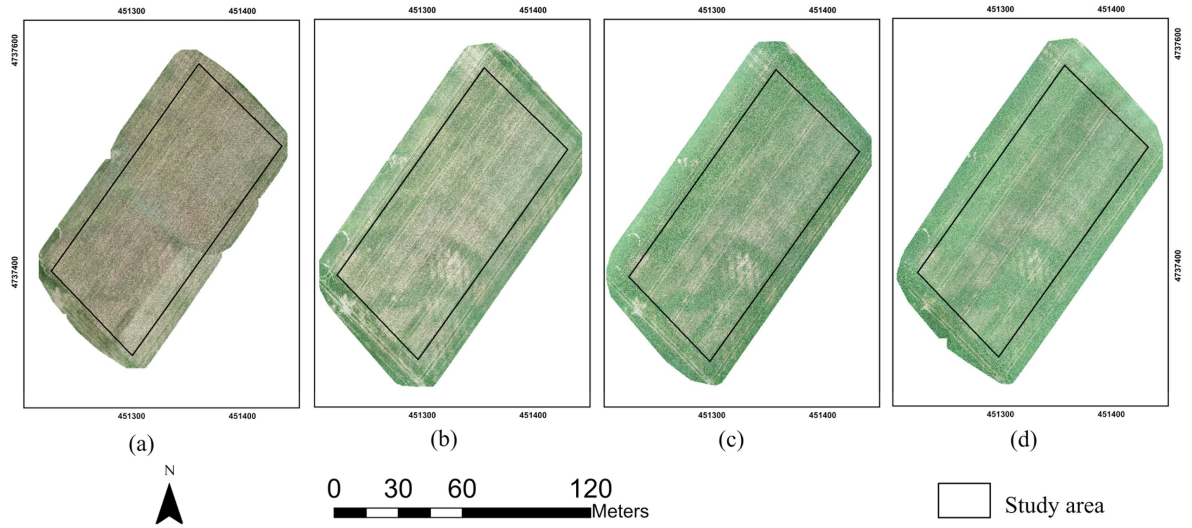

Fig. 2. UAV orthomosaic aerial images for all four growth stages over the study area. (a) May 11 (BBCH = 21). (b) May 21 (BBCH = 31). (c) May 27 (BBCH = 39). (d) June 3 (BBCH = 49).

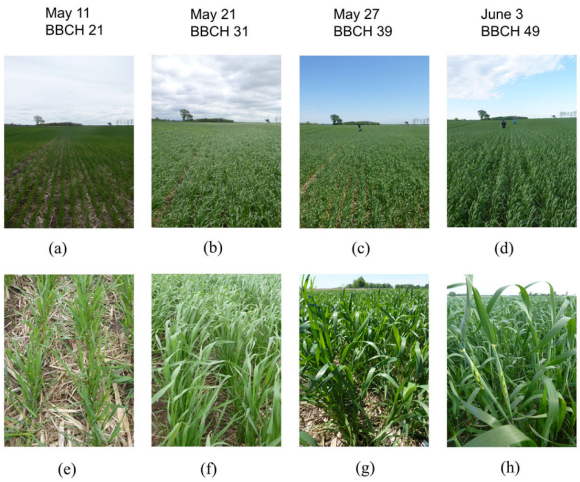

Fig. 3. Landscape and close-up winter wheat photos at four growth stages in the field. (a) and (e) Landscape and close-up images at stage of BBCH 21. (b) and (f) Landscape and close-up images at stage of BBCH 31. (c) and (g) Landscape and close-up images at stage of BBCH 39. (d) and (h) Landscape and close-up images at stage of BBCH 49.

TABLE I
UAV FLIGHT DATA AND CROP GROWTH STAGE

Flight Date	Number of Images	Points in the dataset	Point Density (pts/m^2)	Average LAI_e (m^2/m^2)	Growth Stage (BBCH)
11-May-19	1257	118114965	4299	0.49	Tillering (21)
21-May-19	1157	160528594	5843	0.87	Stem Elongation (31)
27-May-19	1157	179352912	6528	1.14	Stem Elongation (39)
3-Jun-19	1157	171010292	6224	1.22	Booting (49)

pts = point, m = meter, BBCH = Biologische Bundesanstalt, Bundessortenamt und CHemische Industrie.

data from UAV-based imagery using photogrammetry method [36]. The output of the 3-D point cloud dataset has a similar format to LiDAR data, which contains positions and the RGB information at each point. This photogrammetry 3-D point cloud data has a low cost and can still provide structural and optical information of features. Four UAV acquisitions at different crop growth stages were carried out over the winter wheat field on May 11, May 21, May 27, and June 3 in 2019 (see Fig. 2). The phenology of winter wheat represented by BBCH-scales was 21, 31, 39, and 49 on these dates, respectively, covering the leaf development stages for the winter wheat field under investigation [37]. The field landscape and close-up images for these four growth stages are shown in Fig. 3.

All UAV images were captured at the nadir position at the height of 30 m above ground. The overlap of all images was 90% on all sides to ensure the success of image mosaicking on the homogeneous crop canopy. The spatial resolution for all four aerial images is 9 mm. The UAV flight date, number of images, points in the dataset, point density, average ground measurements, and crop phenology are listed in Table I. The images were processed using Pix4Dmapper Pro (Pix4d) v2.4 to generate orthomosaic aerial images and 3-D point cloud datasets. The 3-D point cloud data processing, including data clipping and data format conversion, was conducted in C++ with the point cloud library. The aerial images and close-up winter wheat field photos are shown in Figs. 1 and 2.

D. Simulated Observation of Point Cloud

We developed an approach named simulated observation of point cloud (SOPC) to divide the point cloud data into many slices with different observation zenith angles and investigated the 3-D spatial distribution of points in each slice. A grid of

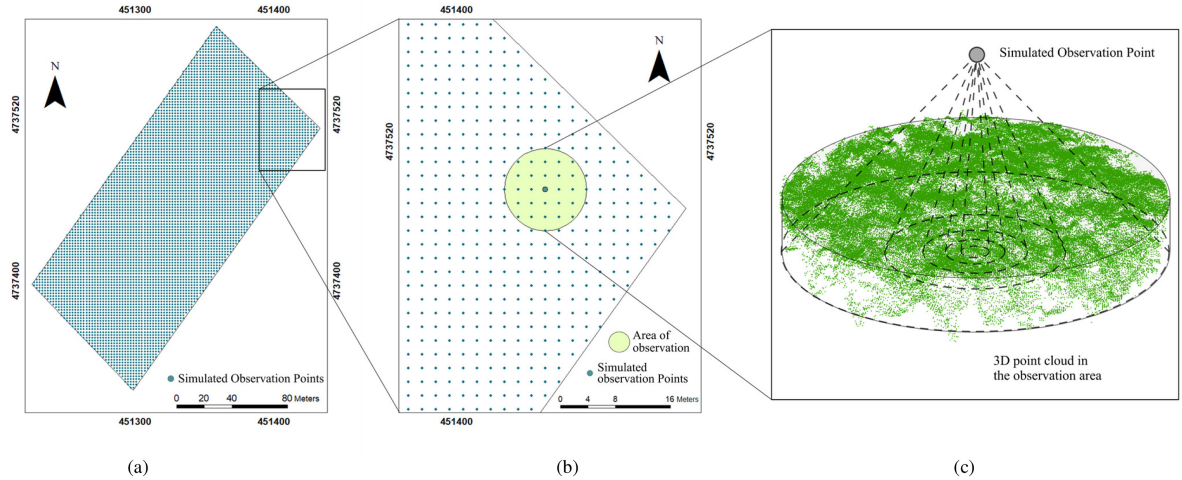

Fig. 4. Locations of simulated observation points and area of observation within the point cloud dataset. (a) Simulated observation points at the resolution of 2 × 2 m. (b) Area of observation for one simulated observation point with a radius of 6 m. (c) 3-D perspective view of the point cloud data in the observation area.

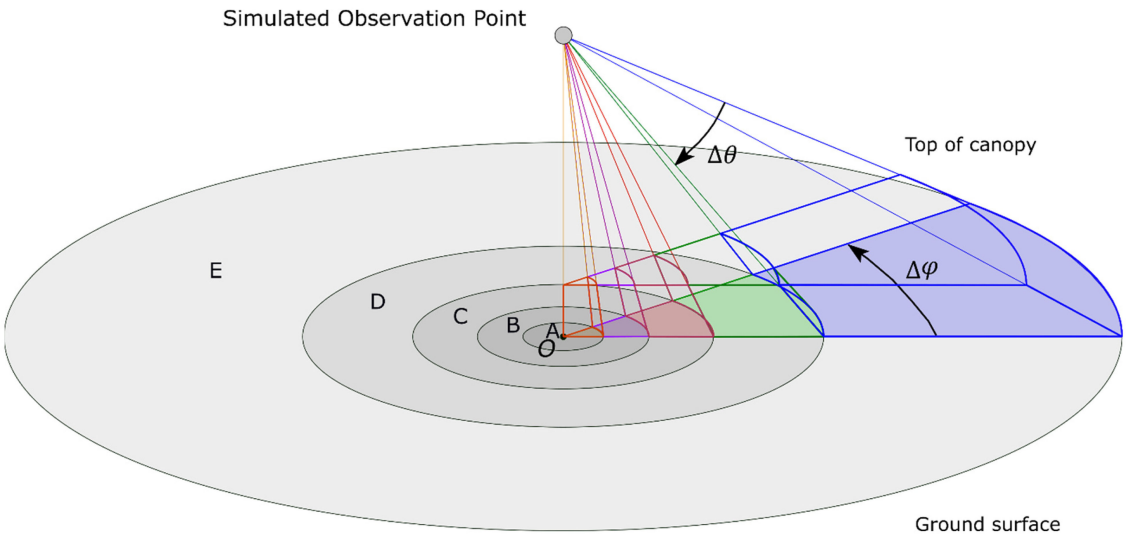

Fig. 5. 3-D schematic of the SOPC for one area of observation. The area of observation is divided into five concentric observation rings A, B, C, D, and E. The observation angle for each ring is $\Delta\theta$. Each observation ring will be divided into many slices with an angle of $\Delta\varphi$.

observation points was generated above the point cloud data with a resolution of 2 × 2 m. This selected resolution of simulated observation points will be used to demonstrate the within-field LAIe variation of the study area. Under the simulated observation point, an area of observation was selected within the point cloud dataset. The size of the area was calculated based on the height of the observation point. Since the ground-based LAIe measurement adopted the height of the fisheye camera is 1 m, the height of simulated observation points was set to 1 m higher than the point cloud data in this study. Each observation point was used as the origin point O to calculate the bounding box of the area of observation. Since the maximum observation angle was 75° in this study, the maximum radius was determined to be 8 m to cover all points within the field of view. The position of observation points and the area of observation are shown in Fig. 4. The projected observation point on the ground is the simulated origin point O for the area of observation. Any point in the point cloud data has a horizontal distance to the origin point O, which is less than 8 m will be selected. A total of 5977 observation areas was generated in this study. From the simulated observation point to the ground surface in each observation area, the field of view was divided into many slices with a certain azimuth and zenith angle. The angles of the slice $\Delta\varphi$ and $\Delta\theta$ on horizontal and vertical directions were 15° in this study for the multiview angles gap fraction method. Five observation rings were generated, and each ring was divided into 24 slices. The points in each slice were then used to calculate the gap fraction. The schematic of SOPC is illustrated using Fig. 5.

E. Gap Fraction Calculation Using UAV-Based 3-D Point Cloud Data

The distribution of vegetation and bare ground points for the winter wheat 3-D point cloud dataset has been described by a

recent UAV-based point cloud study [29]. The bare ground points in a point cloud dataset decrease as the winter wheat grows and disappears after full covered canopy. According to the variation of bare ground points in the point cloud dataset, it is assumed that the vegetation leaf is a black body which has no light penetrating the vegetation points, and the gap fraction could be calculated from the ratio of bare ground points n and the total number of points N in a specific slice at certain view angles of $\Delta\varphi$ and $\Delta\theta$. The greenness of each pixel calculated from the native red, green, and blue color has been used to classify the bare ground and green vegetation from the ground digital images on winter wheat [17]. In this study, the greenness of each point will be calculated for the entire point cloud dataset

$$\text{Greenness} = 2G - B - R \tag{8}$$

where *R*, *G*, and *B* are the intensity values recorded by the UAV camera. Then, the threshold of classification for 5977 observation areas separated from the entire point cloud dataset will be determined individually. Otsu's method was applied to the point cloud data of each observation area to determine the threshold automatically. After classifying the points into vegetation and bare ground, the points will be projected onto a plane surface using different projection techniques for vertical, multiview angles gap fraction methods. The lower point will be removed from the projected plane surface when two points have the same location after projection.

Three methods were developed to calculate vertical, 57.5°, and multiview angle gap fraction in this study.

1) The SOPC vertical gap fraction method (SOPC-V) was used to calculate the vertical gap fraction of crop in the point cloud data. All points in the point cloud data will be projected to the ground surface using parallel projection. After removing the duplicate points on the ground surface, the gap fraction was then calculated from the ratio of bare ground and the total points. Since the vertical gap fraction has a small observation area, the vertical gap fraction was determined based on many 2 × 2 m voxels divided from the point cloud dataset in this study.
2) The SOPC fixed gap fraction (SOPC-F) was used to calculate the 57.5° gap fraction in the point cloud data. After using SOPC to determine the simulated observation points and area, all points in the point cloud data will be projected onto the ground surface using the central projection to remove the duplicate points on the ground. The 57.5° gap fraction will be calculated from the ratio of bare-ground and total points in a specific observation ring which is between the view angles 53° and 61°. The spatial resolution of simulated observation points was 2 × 2 m in this study.
3) The SOPC multiview angle gap fraction (SOPC-M) was used to calculate gap fraction at different observation rings. The central projection will be used to remove duplicate points. The spatial resolution of simulate observation points was set to 2 × 2 m in this study. Ultimately, the LAIe results will be calculated using (2), (3), and (7), respectively. The general flowchart of SOPC method shown in Fig. 6.

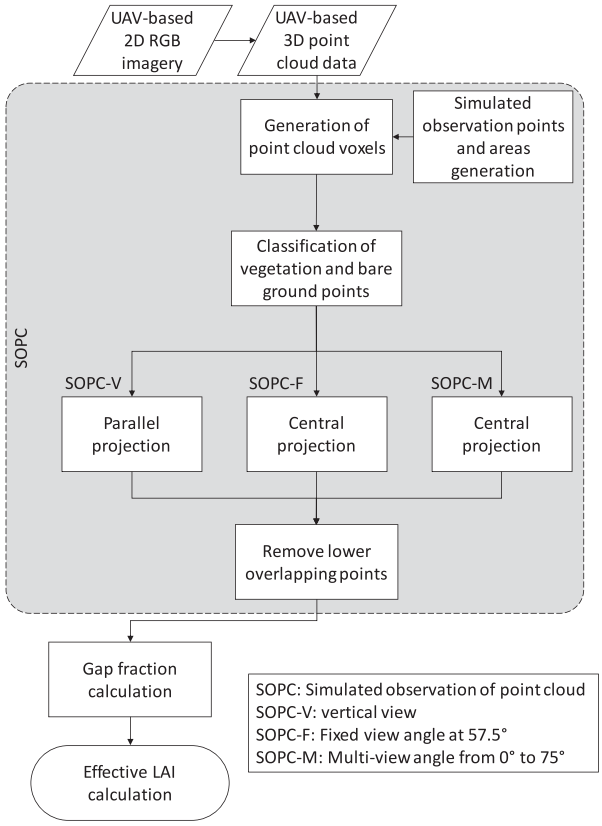

Fig. 6. Flowchart of effective LAI estimation using SOPC methods from UAV-based 3-D point cloud data.

F. Methods Assessment

The *in-situ* LAIe measurements were used to evaluate the accuracy of UAV-based point cloud LAIe in this study. The relationship between *in-situ* and UAV-derived LAIe on multiple dates were used to evaluate the long-term LAIe trend. The root mean square error (RMSE) was used to evaluate the prediction error of LAIe. In addition, the mean absolute error (MAE) was used to evaluate the average magnitude of the LAIe error. For comparison purposes, the map of winter wheat LAIe was generated in this study using the SOPC-V, SOPC-F, and SOPC-M methods. The performances of winter wheat LAIe estimation using the three methods will be compared and discussed in this study.

III. Results

A. Estimation of Effective LAI With the SOPC-V Methods

The relationship between the SOPC-V method derived LAIe using UAV-based 3-D point cloud data and the ground DHP derived LAIe are associated, with an $R^2 = 0.6989$ for all 128 samples (see Fig. 7). The LAIe maps generated using the SOPC-V method are shown in Fig. 8. The overall variation of the LAIe was in the range of 0 to 1.27. Thame maximum, minimum, mean, stand deviation, RMSE, and MAE for all four LAIe maps are listed in Table II. The RMSE of the overall four growth stages is 0.42 and the MAE is 0.38.

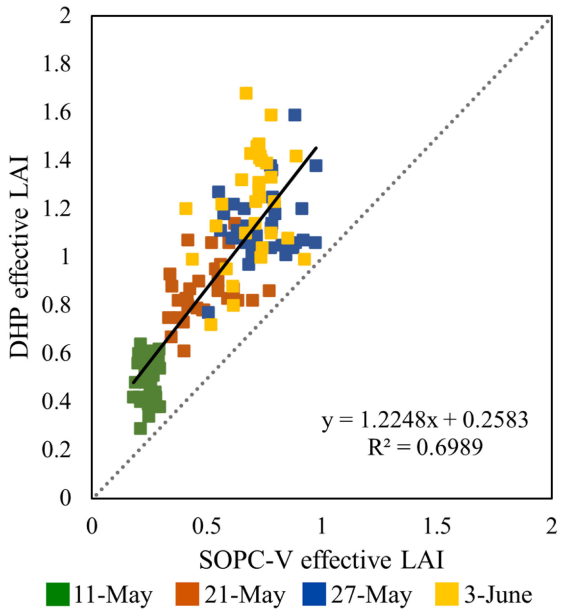

Fig. 7. Comparison between the SOPC-V method derived effective leaf area index (LAIe) and ground DHP derived LAIe. The sampling points were represented by different colors on May 11, May 21, May 27, and June 3. The solid line is the trendline, and the dash line is 1:1 ratio line.

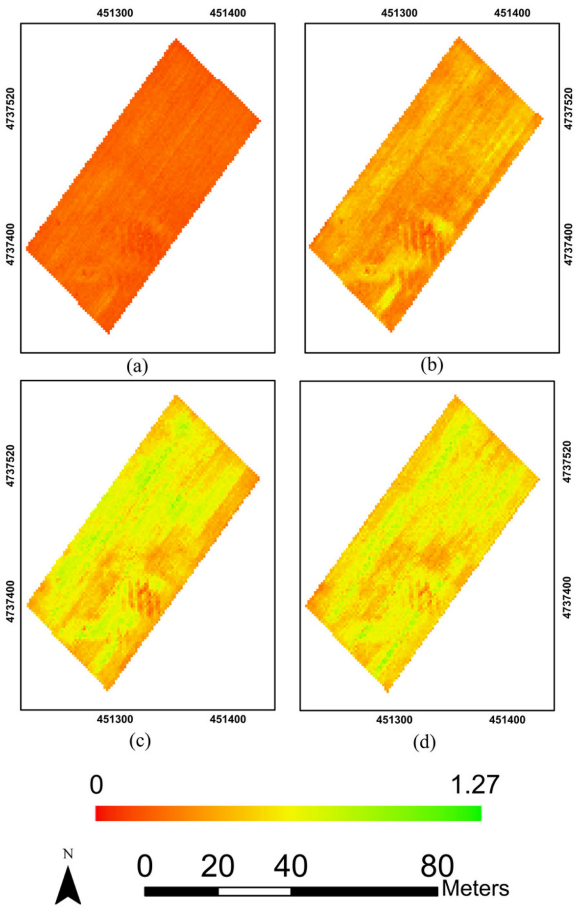

Fig. 8. Effective leaf aera index (LAIe) map generated using the SOPC-V method on UAV-based 3-D point cloud dataset for four growth stages. (a) May 11, BBCH = 21. (b) May 21, BBCH = 31. (c) May 27, BBCH = 39. (d) June 3, BBCH = 49. The scale was normalized from 0 to 1.27.

TABLE II
STATISTIC INFORMATION OF THE SOPC-V METHOD DERIVED EFFECTIVE LAI

	11-May	21-May	27-May	3-Jun	Overall
Maximum	0.44	0.99	1.29	1.27	
Minimum	0.09	0.11	0.20	0.28	
Mean	0.25	0.49	0.73	0.73	
STD	0.04	0.10	0.15	0.13	
Bias	-0.23	-0.37	-0.39	-0.52	
RMSE	0.25	0.39	0.43	0.56	0. 42
MAE	0.18	0.35	0.56	0.41	0.38

The range of LAIe, mean, stand deviation (STD), RMSE, and MAE for all 32 sampling points at different growth stages and the overall study period derived by the SOPC-V method.

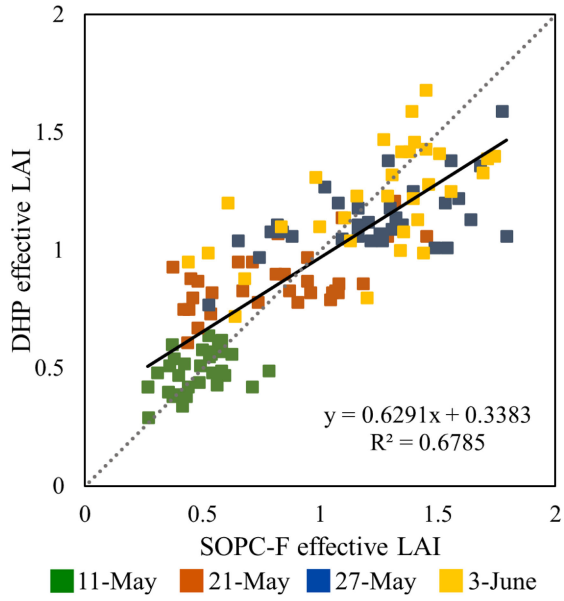

Fig. 9. Comparison between the SOPC-F method derived LAIe and ground DHP derived LAIe. The sampling points were represented by different colors on May 11, May 21, May 27, and June 3. The solid line is the trendline, and the dash line is 1:1 ratio line.

B. Estimation of Effective LAI With the SOPC-F Method

The relationship between the SOPC-F method derived LAIe using UAV-based 3-D point cloud data and the ground DHP derived LAIe are associated, with an $R^2 = 0.6785$ for all 128 samples, which is shown in Fig. 9. The LAI maps generated using the SOPC-F method are shown in Fig. 10. The overall variation of the LAIe was in the range of 0 to 6.43. The maximum LAIe, minimum LAIe, mean LAIe, stand deviation, RMSE, MAE for all four LAIe maps are listed in Table III. The RMSE of the overall four growth stages is 0.24 and MAE was 0.19.

C. Estimation of Effective LAI With the SOPC-M Method

A relationship between the SOPC-M method derived LAIe using the UAV-based point cloud data and LAIe derived from DHP captured by the fisheye camera is shown in Fig. 11. The estimated LAIe values are highly correlated with the ground fisheye derived LAIe value, $R^2 = 0.7621$, for 128 samples, which includes the data from May 11 to June 3. The R^2 was 0.7646

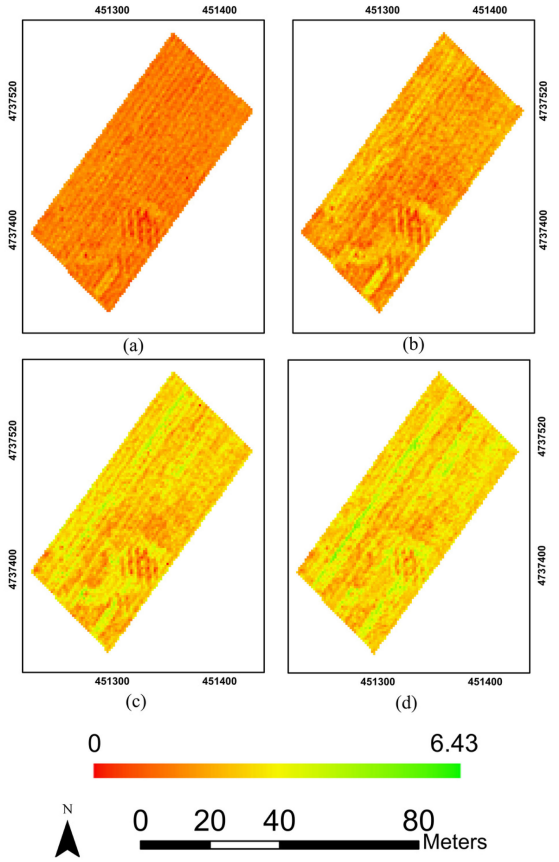

Fig. 10. LAIe map generated using the SOPC-F method on UAV-based 3-D point cloud dataset for four growth stages. (a) May 11, BBCH = 21. (b) May 21, BBCH = 31. (c) May 27, BBCH = 39. (d) June 3, BBCH = 49. The scale was normalized from 0 to 6.43.

TABLE III
STATISTIC INFORMATION OF THE SOPC-F METHOD DERIVED EFFECTIVE LAI

	11-May	21-May	27-May	3-Jun	Overall
Maximum	1.32	2.78	4.68	5.54	
Minimum	0.01	0.06	0.11	0.12	
Mean	0.46	0.75	1.29	1.44	
STD	0.14	0.32	0.54	0.62	
Bias	-0.01	-0.06	0.09	0.01	
RMSE	0.12	0.25	0.29	0.27	0.24
MAE	0.09	0.22	0.24	0.22	0.19

The range of LAIe, mean, stand deviation (STD), RMSE, and MAE for all 32 sampling points at different growth stages and the overall study period derived by the SOPC-F method.

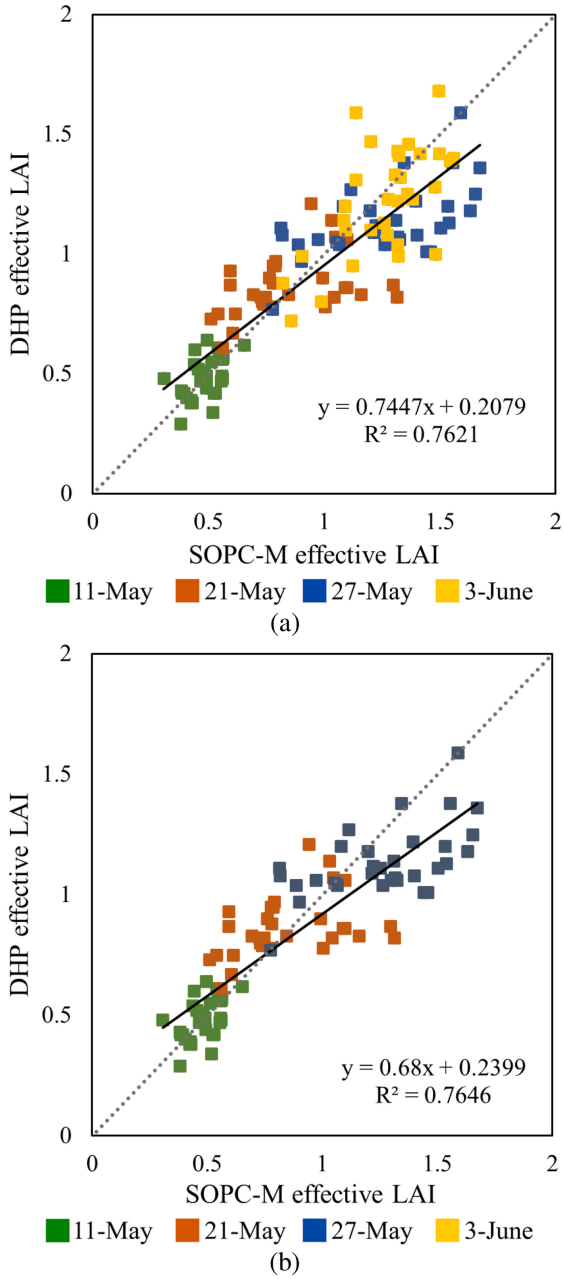

Fig. 11. Relationship between the SOPC-M method derived LAIe using UAV-based 3-D point cloud data and ground DHP derived effective LAI. (a) All points from May 11 to June 3. (b) All points from May 11 to May 27. The sampling points were represented by different colors on May 11, May 21, May 27, and June 3. The solid line is the trendline, and the dash line is 1:1 ratio line.

for all 96 samples from May 11 to June 27. After applying the SOPC-M method to calculate LAIe on the UAV-based point cloud dataset, four LAIe maps of the winter wheat at different growth stages are shown in Fig. 12. In this figure, the LAIe value has been normalized to the same scale from 0 to 4.3.

D. SOPC-M Effective LAI Maps at Different Winter Wheat Growth Stages

The LAIe within-field variation maps from the early growth stage (BBCH 21) to the full leave growth stages (BBCH 61) are displayed in Fig. 13. The average values of LAIe were 0.48, 0.78, 1.31, and 1.46 on May 11, May 21, May 27, and June 3 respectively. To show the accuracy of this method, the RMSE and MAE were compared between the SOPC-M LAIe and ground-based DHP derived LAIe for all 32 sampling points at all four growth stages. The RMSE was 0.08 on May 11, 0.20 on May 21, 0.25 on May 27, and 0.19 on June 3; the overall RMSE for all four growth stages was 0.19. The MAE was 0.06 on May 11, 0.16 on May 21, 0.21 on May 27, and 0.15 on June 3; the overall MAE was 0.14. The maximum, minimum, mean, stand deviation, RMSE, and MAE of the estimation LAIe results for all four maps are listed in Table IV.

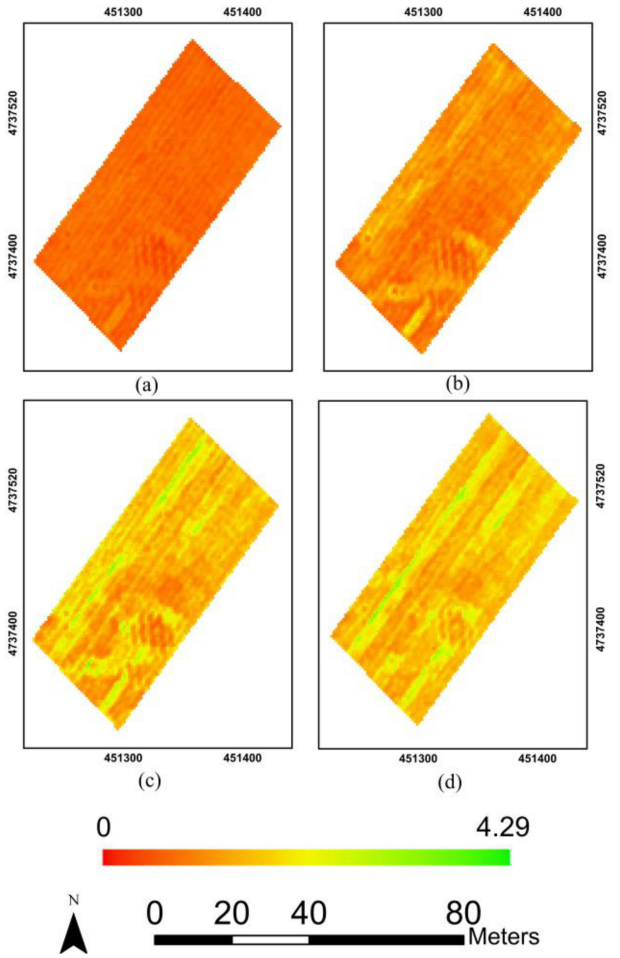

Fig. 12. LAIe map generated using the SOPC-M on UAV-based 3-D point cloud dataset for four growth stages. (a) May 11, BBCH = 21. (b) May 21, BBCH = 31. (c) May 27, BBCH = 39. (d) June 3, BBCH = 49. The scale was normalized from 0 to 4.29.

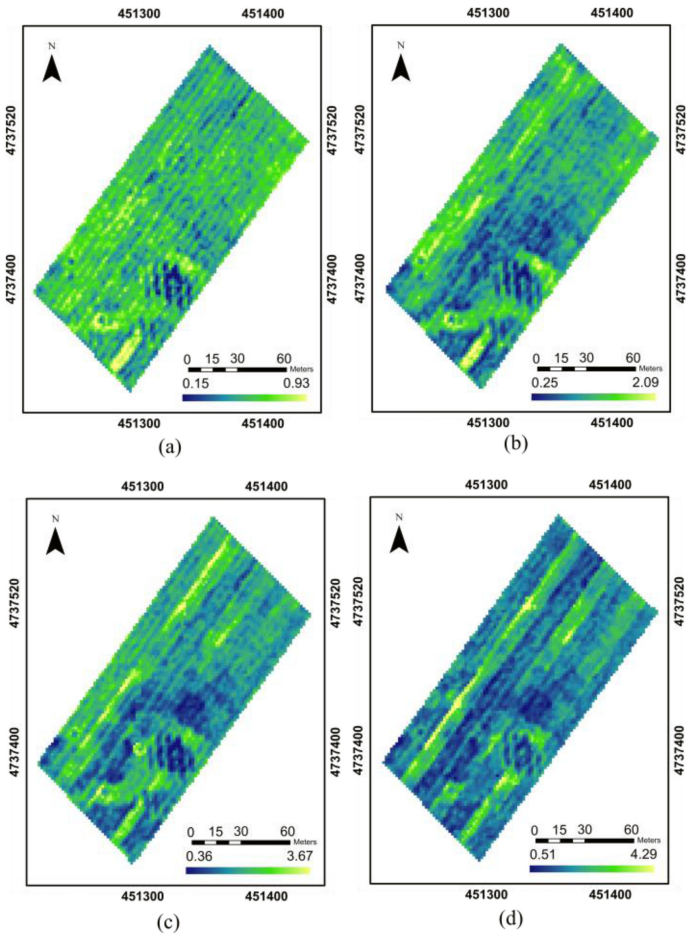

Fig. 13. Individual winter wheat LAIe maps using SOPC-M method at different growth stages. (a) May 11. (b) May 21 (c) May 27. (d) June 3.

IV. Discussion

A. Comparisons Between SOPC-V, SOPC-F, and SOPC-M Methods Derived Effective LAI Estimates

The greenness of each pixel calculated from the native red, green, and blue color has been used to classify the bare ground and green vegetation from the ground digital images on winter wheat [20]. In this study, the study area was divided into 5977 observation areas, and the threshold for each observation area was determined individually. Otsu's method was applied on point cloud data of each observation area to determine the threshold automatically. New classification methods or more spectral information could be considered in future studies to improve the efficiency and accuracy in the determination of threshold.

A comparison among the SOPC-V, SOPC-F, and SOPC-M methods had been performed on UAV-based point cloud data. They were compared against the ground-based DHP LAIe results and their relationships are shown in Figs. 7, 9, and 11. The SOPC-V and SOPC-F methods derived LAIe had a similar coefficient of determinations, which were lower than the SOPC-M method derived LAIe. The SOPC-V measured the gap fraction from 2-D perspectives; SOPC-F method measured gap fraction from 3-D perspectives at a certain view angle. In contrast, the SOPC-M method used the maximum gap fraction information at multiple view angles, which is like the DHP method in considering the integrated gap fraction of crop canopy. The comparison of the coefficient of determination for these

TABLE IV
Statistic Information of the SOPC-M Method Derived Effective LAI

	May 11	May 21	May 27	June 3	Overall (May 11 to June 3)	Overall (May 11 to May 27)
Maximum	0.92	2.09	3.67	4.29		
Minimum	0.15	0.25	0.36	0.51		
Mean	0.48	0.78	1.31	1.46		
STD	0.09	0.23	0.39	0.48		
Bias	-0.001	-0.02	0.13	0.04		
RMSE	0.08	0.20	0.25	0.19	0.19	0.19
MAE	0.06	0.16	0.21	0.15	0.14	0.14

The range of LAIe, mean, stand deviation (STD), RMSE, and MAE for all 32 sampling points at different growth stages and the overall study period derived by the SOPC-M method.

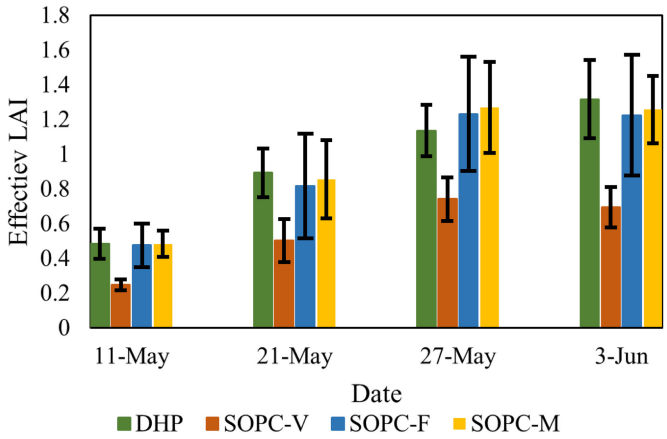

Fig. 14. Error bars of all SOPC and DHP methods on May 11, May 21, May 27, and June 3. The column bars represent the mean values of LAIe, and the error bars represent the upper and lower limit of the errors.

three methods was challenging to indicate the performance of all three methods in LAIe estimation due to that the SOPC-V and F are based on different principles from the DHP method. However, the relationship between the SOPC and DHP methods derived LAIe demonstrated the potential of the SOPC method in LAIe estimation using the UAV-based point cloud data. The actual LAI retrieved from the destructive method or measured from LAI-2000 could be used in future studies to better evaluate the performances of the three SOPC methods.

According to Tables II–IV, the SOPC-V had a larger bias with consistently smaller LAIe values than the DHP method, whereas the SOPC-F and M methods had a similar small bias. Fig. 14 displays the uncertainty of all three SOPC methods compared with the DHP method. The SOPC-V method had the smallest uncertainty which is as large as the DHP method. The SOPC-F method had the largest uncertainty among three SOPC methods for all four dates. The SOPC-M and the DHP method had similar uncertainties and smaller bias. In addition, the mean of LAIe for SOPC and DHP methods increased significantly from May 11 to May 27 (see Fig. 14). For the booting stage (June 3), the mean of LAIe for SOPC methods decreased. In contrast, the DHP method derived means of LAIe increased continuously. Therefore, the LAIe map on June 3 had more noisy estimations. The lower mean value on June 3 for all three SOPC methods indicated the limitation on LAI estimations at the booting stage.

Shadow effect could be one of the reasons limiting the LAIe estimation in the later growth stages using UAV-based point cloud data. Although all UAV flights were performed between 10 A.M. and 2 P.M. to reduce the shadow effects in the field, the shadow can still be observed on the images. In the winter wheat field, shadow pixels can be observed from two categories: one is the leaf shadow projected on the bare ground, and the other is the leaf shadow projected on other leaves within the crop canopy, which has a small area in the images. Small shadow areas observed from different directions may have shape distortion in the UAV-based imagery, which is difficult to match and generate the shadow points in the point cloud data. Fig. 15 shows the UAV-based point cloud data and the UAV imagery at the same

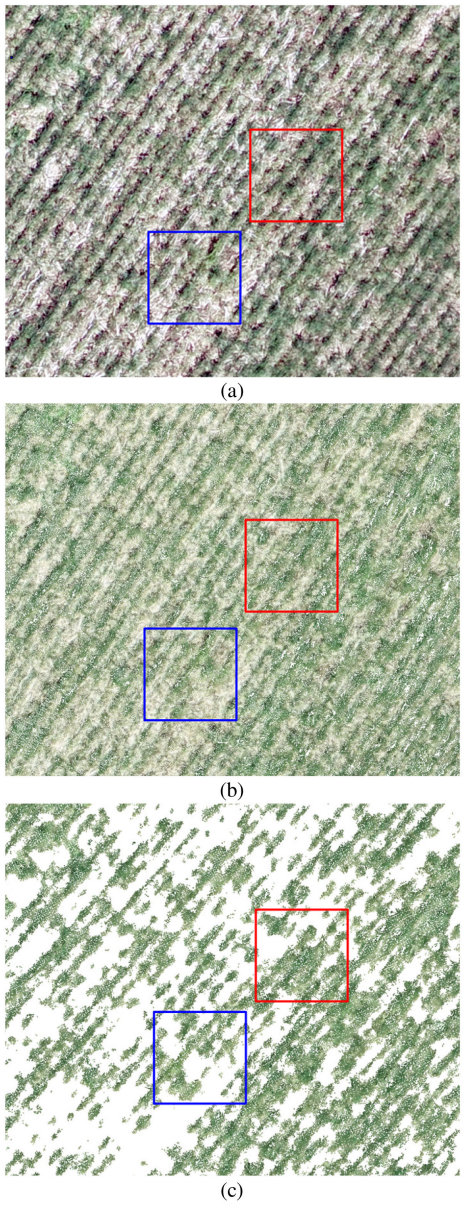

Fig. 15. Illustrate of shadow in winter wheat on May 21. (a) UAV image. (b) UAV-based point cloud data. (c) Vegetation points after point cloud classification. The shadows within the canopy and on the ground are shown in the red and blue blocks.

location in the field. The small shadow areas were significantly reduced in the UAV-based point cloud data [see Fig. 15(b)]. The removal of small shadow areas will reduce the size of vegetation and bare ground points leading to inaccurate LAIe estimation. In addition, the classification method using the greenness feature can effectively extract the green leaves in both sunlit and shaded conditions for winter wheat in the early growth stage before canopy closure [20]. The large shadow areas were treated as the bare ground point after classifying the point cloud data [see Fig. 15(c)].

In our study site, the winter wheat rows had an east-west direction, which will ensure the plants in a row obtain the sunlight from the south direction, and the shadow appears on

the north side of the crop row. The angles of facing against and facing away from the sun were different due to the difference in imaging time on the day of the UAV operation. The UAV flights were operated at 10:40 A.M., 12:30 P.M., 10:40 A.M., and 1:20 P.M. on May 11, May 21, May 27, and June 3, the azimuth angles of the sun and shadow were different on these dates. The gap fraction at different observation angles was evaluated to analyze the illumination influence in the UAV-based point cloud data. Fig. 16 shows the gap fraction at different observation angles (φ). The dash lines represent four sampling points selected from each sampling row, and the solid line represents the average gap fraction for all 32 samples in the field. The gray and blue bars represent the position of the sun and shadow. After comparing all 32 sampling points on all four monitoring dates, the average gap fractions at the angles of facing against and facing away from the sun were very close. The values of gap fraction do not vary significantly at different observation angles. The illumination effect on gap fraction measurements on the UAV-based point cloud data is not significant.

Data resolution could be another factor influencing the LAIe estimation in the booting stage using the UAV-based point cloud data. During the ground data collection, the DHP was captured at one meter above the canopy. The center of the DHP has a resolution of 0.3 mm, which can easily capture the shaded leaves under the crop canopy. More shaded leaf pixels can be correctly extracted using the high-resolution DHP images. The UAV-based point cloud data contains 0.4 million points for the simulate observation area, but the point has the same resolution as the pixel in the image captured by the UAV, which is 1 cm. At this resolution, the shaded leaves within the canopy will be treated as shadows. The unmatched shadow area within the crop canopy will produce empty spots in the point cloud data and generate fewer vegetation points. The fewer vegetation points will lead to a lower LAIe estimation in the later growth stage with a dense canopy. For example, the ratios of the vegetation and the total points in the observation area before the projection for sampling point 12 on May 11, May 21, May 27, and June 3 were 8%, 38%, 72%, and 75%. The average ratio of the vegetation and the total number of pixels on the DHP images were 23%, 46%, 54%, and 63%. After reducing the resolution of the DHP images into the resolution of 1 cm, the ratio changed to 29%, 43%, 50%, and 54%. The percentage of vegetation pixels has a smaller increase rate at the resolution of 1 cm because the shaded vegetation pixel merged with the shadow pixels together. The same observation was obtained in the UAV-based point cloud data. The vegetation points slightly increased in the booting stage, and the estimation of LAIe tends to be saturated at this growth stage using the SOPC methods.

In addition, the portion of vegetation and bare ground points will change from the emergence stage to the heading stages of winter wheat. The histogram of the points distribution shows only one peak, which was composed of vegetation points only in an individual voxel when the crop canopy closed [29]. In this case, the determination of bare ground points is challenging and produces the incorrect LAIe estimation in the later growth stage. Since the LAI of the crop should gradually increase over time during the leaf development stages, the percentage of the lower

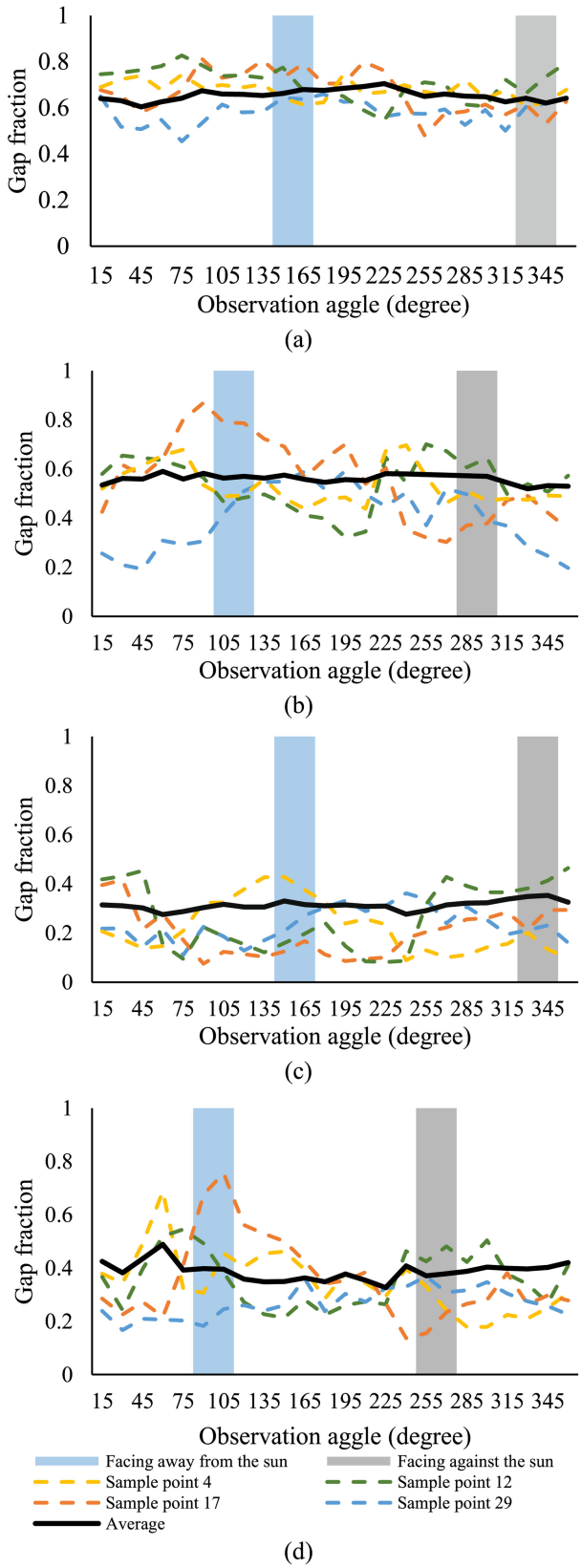

Fig. 16. Values of gap fraction at different observation angles for four sampling points on May 11, May 21, May 27, and June 3. (a) May 11. (b) May 21. (c) May 27. (d) June 3. The gray and blue rectangles represent the observation angles facing against and facing away from the sun at the specific time on the monitoring day. The solid black line represents the average gap fraction for 32 sampling points.

TABLE V
LOWER EFFECTIVE LAI ESTIMATION ON MAY 27 AND JUNE 3

	SOPC-V	SOPC-F	SOPC-M	DHP
27-May	3.73%	7.50%	0.50%	0%
3-Jun	51.83%	46.26%	33.68%	28.12%

The percentage of lower effective LAI estimation on May 27 and June 3.

LAIe estimation compared with the previous monitoring was evaluated on both LAIe maps and DHP ground measurements on May 27 and June 3. The amount of lower LAIe estimations was calculated by subtracting the LAIe estimation of a later date. The percentage of the lower LAIe estimation on LAIe maps was calculated by the ratio of the amount of lower LAIe and the total pixel number of 5977. The percentage of the lower LAIe for DHP method was calculated by the ratio of the number of lower LAIe and the total sampling points. The results of all three SOPC and DHP methods are listed in Table V. According to the results, the amount of lower LAIe estimations increased substantially on June 3 for SOPC and DHP methods. Among the three SOPC methods, the SOPC-M had the lowest percentage of lower LAIe estimation on May 27 and June 3, which were 0.50% and 33.68%, respectively. The DHP had a lower percentage of lower LAIe than the SOPC-M method which is 0% and 28.12% on May 27 and June 3. However, while the evaluation of the DHP method is based on the 32 ground sampling points, the percentage may change if applicable to the entire study site.

Furthermore, the SOPC-F and SOPC-M methods generated higher LAIe estimations around the tractor wheel tracks in the study area on the map of June 3. It is because these two methods monitored the canopy with a view angle which had a larger observation area than the SOPC-V method. The tracker wheels compacted the soil and destroyed the plants and left open areas in the field. The open area promoted the growth of crop near it and helped to produce a more accurate classification for bare ground points, which lead to a higher LAIe estimation than the area with full canopy on June 3 using the SOPC-V and SOPC-M methods.

B. Advantages and Limitations of the SOPC Method

One of the most advantageous aspects of the SOPC method is that it can be used to calculate LAIe directly from the point cloud data without the requirement of ground-based reference LAI measurements. This could greatly reduce the time and resources for taking ground LAI measurements. Second, this method can provide a much larger number of field samples in comparison with the field-based method. For instance, more than five thousand LAI estimates were generated in this study. Third, this method can provide multiscale maps by modifying the resolution of observation points, which can meet different agricultural application requirements. Furthermore, UAV derived point cloud data collected from one flight can also be used to retrieve other crop physical parameters such as canopy height and biomass, hence making UAV-derived point cloud data very cost-efficient.

The SOPC method does not require image calibration to normalize the dataset for multitemporal imagery acquisitions. Another economic benefit of the SOPC method is that it uses a regular high-resolution RGB camera for imaging, leading to lower cost than that of a multispectral camera in data collection. Unlike multispectral images, the regular images do not require alignment correction for multiple bands in the multispectral image dataset.

Like all other methods, SOPC also has its disadvantages. One shortcoming is large time consumption when generating the point clouds. This step relies heavily on computer power. For this study, it took 30 h to generate the point cloud and calculate the LAIe for one of the four acquisition dates using a computer system equipped with a 12-core XEON processor and Quadro M4000 graphic card. Benefit from the rapid development of technology, including commercial cloud service providers are now offering high-speed data processing, which will result in much reduced computer time. Another disadvantage of the UAV method is its limitation in area of coverage due to the requirements of the 30-m flying altitude the ground and a very high image overlapping rate to collect super-high-resolution images. As a result, mapping LAI for large fields will take a long time to fly and abundant space for image storage. However, these barriers will likely be overcome in the near future.

C. Application

The proposed SOPC-M method uses the ratio of bare ground and the total number of points in a simulated observation area to calculate the gap fraction and LAIe for a winter wheat field. Although the structure of wheat canopy is complex, this method was able to retrieve the LAIe estimation using point cloud data containing both vegetation and bare ground information. The resultant LAIe maps revealed nicely the within-field variation of the winter wheat. This method can successfully be applied to LAIe monitoring and estimation between leaf development and the stem elongation stages as shown through this study (BBCH 20-39). LAI information from these stages is valuable for winter wheat growth modeling and final grain yield forecast [30]. The information of LAIe could help end-users identify the growth status of crops and make early decisions on agricultural management strategies. The UAV-based 3-D point cloud data derived LAIe could be an alternative to LAI monitoring during the canopy development stages. However, the performance of the proposed method declines when estimating LAIe at late growth stages once the crop canopy is fully developed. As revealed by the results from this study, the average estimated LAIe value did not show much variation after the booting stage for winter wheat due to the limitation of point classification at full canopy cover. Improved point classification methods need to be developed and tested in future studies to extend the LAIe estimation to later growth stages of crops. In addition, the UAV-derived LAIe method should be evaluated for other crops such as corn and soybean having different leaf structure and distribution.

V. CONCLUSION

In this study, we have developed the LAIe estimation methods at the subfield scale using UAV-based 3-D point cloud data

in a winter wheat field. The following conclusions have been reached.

1) The SOPC methods using UAV-based 3-D point cloud data could be used to estimate crop LAIe based on a gap fraction method instead of the traditional optical VI methods in the leaf development stage.
2) The SOPC methods derived LAIe tends to be saturated at a higher LAIe value which is greater than 1.5.
3) The SOPC-M method had a better agreement with downward-looking DHP image-based estimates during the leaf development stages (BBCH 20-39). The estimated LAIe has the potential of being used as a reference in many other applications.
4) The SOPC-M method can effectively identify within-field LAIe variation for early monitoring of crop growth conditions, which is useful for making timely management decisions.

ACKNOWLEDGMENT

The authors would like to thank B. Shan, C. Liao, Q. Xie, M. Xing, and D. Wang for their help in field data collection. The authors would also like to thank A&L Canada Laboratories Inc., for providing the study field in London Ontario.

REFERENCES

[1] G. Zheng, L. M. Moskal, and S. H. Kim, "Retrieval of effective leaf area index in heterogeneous forests with terrestrial laser scanning," *IEEE Trans. Geosci. Remote Sens.*, vol. 51, no. 2, pp. 777–786, Feb. 2013.

[2] E. J. Botha, B. Leblon, B. Zebarth, and J. Watmough, "Non-destructive estimation of potato leaf chlorophyll from canopy hyperspectral reflectance using the inverted PROSAIL model," *Int. J. Appl. Earth Observation GeoInf.*, vol. 9, no. 4, pp. 360–374, 2007.

[3] X. Jin, Z. Li, H. Feng, Z. Ren, and S. Li, "Deep neural network algorithm for estimating maize biomass based on simulated Sentinel 2A vegetation indices and leaf area index," *Crop J.*, vol. 8, pp. 87–97, 2019.

[4] J. Liu, E. Pattey, J. R. Miller, H. McNairn, A. Smith, and B. Hu, "Estimating crop stresses, aboveground dry biomass and yield of corn using multi-temporal optical data combined with a radiation use efficiency model," *Remote Sens. Environ.*, vol. 114, no. 6, pp. 1167–1177, 2010.

[5] A. Huete, K. Didan, T. Miura, E. P. Rodriguez, X. Gao, and L. G. Ferreira, "Overview of the radiometric and biophysical performance of the MODIS vegetation indices," *Remote Sens. Environ.*, vol. 83, no. 1–2, pp. 195–213, 2002.

[6] D. Haboudane, J. R. Miller, E. Pattey, P. J. Zarco-Tejada, and I. B. Strachan, "Hyperspectral vegetation indices and novel algorithms for predicting green LAI of crop canopies: Modeling and validation in the context of precision agriculture," *Remote Sens. Environ.*, vol. 90, no. 3, pp. 337–352, 2004.

[7] J. Shang *et al.*, "Mapping spatial variability of crop growth conditions using RapidEye data in Northern Ontario, Canada," *Remote Sens. Environ.*, vol. 168, pp. 113–125, 2015.

[8] A. Kross, H. McNairn, D. Lapen, M. Sunohara, and C. Champagne, "Assessment of RapidEye vegetation indices for estimation of leaf area index and biomass in corn and soybean crops," *Int. J. Appl. Earth Observation GeoInf.*, vol. 34, no. 1, pp. 235–248, 2015.

[9] J. Qi *et al.*, "Leaf area index estimates using remotely sensed data and BRDF models in a semiarid region," *Remote Sens. Environ.*, vol. 73, no. 1, pp. 18–30, 2000.

[10] G. Zheng and L. M. Moskal, "Retrieving leaf area index (LAI) using remote sensing: Theories, methods and sensors," *Sensors (Basel, Switzerland)*, vol. 9, no. 4, pp. 2719–45, 2009.

[11] E. R. Hunt, W. D. Hively, C. S. Daugtry, and G. W. McCarty, "Remote sensing of crop leaf area index using unmanned airborne vehicles," in Proc. 17th William T. Pecora Memorial Remote Sensing Symp., 2008, pp. 18–20.

[12] X. Yao *et al.*, "Estimation of wheat LAI at middle to high levels using unmanned aerial vehicle narrowband multispectral imagery," *Remote Sens.*, vol. 9, no. 12, 2017, Art. no. 1304.

[13] X. Zhou *et al.*, "Predicting grain yield in rice using multi-temporal vegetation indices from UAV-based multispectral and digital imagery," *ISPRS J. Photogramm. Remote Sens.*, vol. 130, pp. 246–255, 2017.

[14] P. Propastin and O. Panferov, "Retrieval of remotely sensed LAI using Landsat ETM+ data and ground measurements of solar radiation and vegetation structure: Implication of leaf inclination angle," *Int. J. Appl. Earth Observation GeoInf.*, vol. 25, no. 1, pp. 38–46, 2013.

[15] K. R. Thorp *et al.*, "Estimating crop biophysical properties from remote sensing data by inverting linked radiative transfer and ecophysiological models," *Remote Sens. Environ.*, vol. 124, pp. 224–233, 2012.

[16] C. Atzberger and K. Richter, "Spatially constrained inversion of radiative transfer models for improved LAI mapping from future Sentinel-2 imagery," *Remote Sens. Environ.*, vol. 120, pp. 208–218, 2012.

[17] C. Atzberger *et al.*, "Comparative analysis of different retrieval methods for mapping grassland leaf area index using airborne imaging spectroscopy," *Int. J. Appl. Earth Observation GeoInf.*, vol. 43, pp. 19–31, 2015.

[18] H. Kimm *et al.*, "Deriving high-spatiotemporal-resolution leaf area index for agroecosystems in the U.S. Corn Belt using Planet Labs CubeSat and STAIR fusion data," *Remote Sens. Environ.*, vol. 239, 2020, Art. no. 111615.

[19] M. Weiss, F. Baret, G. J. Smith, I. Jonckheere, and P. Coppin, "Review of methods for *in situ* leaf area index (LAI) determination Part II. Estimation of LAI, errors and sampling," *Agricultural Forest Meteorol.*, vol. 121, pp. 37–53, 2004.

[20] J. Liu and E. Pattey, "Retrieval of leaf area index from top-of-canopy digital photography over agricultural crops," *Agricultural Forest Meteorol.*, vol. 150, no. 11, pp. 1485–1490, 2010.

[21] F. Baret, B. de Solan, R. Lopez-Lozano, K. Ma, and M. Weiss, "GAI estimates of row crops from downward looking digital photos taken perpendicular to rows at 57.5° zenith angle: Theoretical considerations based on 3D architecture models and application to wheat crops," *Agricultural Forest Meteorol.*, vol. 150, no. 11, pp. 1393–1401, 2010.

[22] J. Liu, E. Pattey, and S. Admiral, "Assessment of *in situ* crop LAI measurement using unidirectional view digital photography," *Agricultural Forest Meteorol.*, vol. 169, pp. 25–34, 2013.

[23] M. Weiss and F. Baret, "CAN-EYE v6.4.91 user manual," 2017.

[24] G. W. Frazer, "Gap Light Analyzer (GLA): Imaging software to extract canopy structure and gap light transmission indices from true-colour fisheye photographs. Users manual and program documentation, Version 2.0," Burnaby, BC, Canada, 1999.

[25] G. Zheng, L. Ma, W. He, J. U. H. Eitel, L. M. Moskal, and Z. Zhang, "Assessing the contribution of Woody materials to forest angular gap fraction and effective leaf area index using terrestrial laser scanning data," *IEEE Trans. Geosci. Remote Sens.*, vol. 54, no. 3, pp. 1475–1487, Mar. 2016.

[26] S. Hancock *et al.*, "Characterising forest gap fraction with terrestrial lidar and photography: An examination of relative limitations," *Agricultural Forest Meteorol.*, vol. 189–190, pp. 105–114, 2014.

[27] S. Z. Luo, C. Wang, G. Bin Zhang, X. H. Xi, and G. C. Li, "Forest leaf area index (LAI) inversion using airborne LiDAR data," *ActaGeophysicaSinica*, vol. 56, no. 5, pp. 1467–1475, 2013.

[28] K. Zhao and S. Popescu, "Lidar-based mapping of leaf area index and its use for validating GLOBCARBON satellite LAI product in a temperate forest of the southern USA," *Remote Sens. Environ.*, vol. 113, no. 8, pp. 1628–1645, 2009.

[29] Y. Song and J. Wang, "Winter wheat canopy height extraction from UAV-based point cloud data with a moving cuboid filter," *Remote Sens.*, vol. 11, no. 10, pp. 10–14, 2019.

[30] M. Weiss and F. Baret, "Using 3D point clouds derived from UAV RGB imagery to describe vineyard 3D macro-structure," *Remote Sens.*, vol. 9, no. 2, 2017, Art. no. 111.

[31] B. Pekin and C. Macfarlane, "Measurement of crown cover and leaf area index using digital cover photography and its application to remote sensing," *Remote Sens.*, vol. 1, no. 4, pp. 1298–1320, 2009.

[32] J. B. Miller, "A formula for average foliage density," *Australian J. Botany*, vol. 15, no. 1, pp. 141–144, 1967.

[33] J. M. Welles and S. Cohen, "Canopy structure measurement by gap fraction analysis using commercial instrumentation," *J. Exp. Botany*, vol. 47, no. 9, pp. 1335–1342, 1996.

[34] J. Liu, E. Pattey, and G. Jégo, "Assessment of vegetation indices for regional crop green LAI estimation from Landsat images over multiple growing seasons," *Remote Sens. Environ.*, vol. 123, pp. 347–358, 2012.

[35] J. Shang *et al.*, "Estimating plant area index for monitoring crop growth dynamics using Landsat-8 and RapidEye images," *J. Appl. Remote Sens.*, vol. 8, no. 1, pp. 085196, 2014.
[36] Pix4D, "Drone Mapping Software," *Swiss Federal Institute of Technology Lausanne, Route Cantonale, Switzerland*, 2014.
[37] P. D. Lancashire *et al.*, "A uniform decimal code for growth stages of crops and weeds," *Ann. Appl. Biol.*, vol. 119, no. 3, pp. 561–601, 1991.

Yang Song (Student Member, IEEE) received the B.Sc. degree in environmental practice from the Royal Road University, Victoria, BC, Canada, in 2012, and the M.Sc. degree in geography from the University of Western Ontario, London, ON, Canada, in 2016. He is currently working toward the Ph.D. degree with the Department of Geography, the University of Western Ontario, London, ON, Canada.

His research interest focuses on the application of UAV-based point cloud data for crop field monitoring.

Jinfei Wang (Member, IEEE) received the B.S. and M.Sc. degrees from Peking University, Beijing, China, in 1982 and 1984, respectively, and the Ph.D. degree in geography from University of Waterloo, Waterloo, ON, Canada, in 1989.

She is currently a Professor with the Department of Geography, the University of Western Ontario, London, ON, Canada. Her research interests include methods for information extraction from high resolution remotely sensed imagery, land use and land cover monitoring in urban environments and agricultural crop monitoring using multiplatform multispectral, hyperspectral, Lidar and radar data, and unmanned aerial vehicle data.

Jiali Shang (Member, IEEE) received the B.Sc. degree in geography from Beijing Normal University, Beijing, China, the M.A. degree in geography from University of Windsor, Windsor, ON, Canada, and the Ph.D. degree in environmental remote sensing from University of Waterloo, Waterloo, ON, Canada.

She is a Research Scientist with the Ottawa Research and Development Centre of Agriculture and Agri-Food Canada and Adjunct Professor with York University, Toronto, ON, Canada, and Nipissing University, North Bay, ON, Canada. She has been actively involved in the methodology development and application of earth observation (EO) technology to vegetation biophysical parameter retrieval, crop growth modeling, precision farming, and the detection of field operation activity related to crop production using both optical and radar EO data. In addition to her own research, she is also actively involved in student education, postdoc supervision, and international scientific collaborations.